

Analysis of the performance of the Hartmann–Shack sensor in the human eye

Pedro M. Prieto and Fernando Vargas-Martín

Laboratorio de Optica, Departamento de Física, Universidad de Murcia, Campus de Espinardo (Edificio C), 30071 Murcia, Spain

Stefan Goetz

Institute for Applied Physics, University of Heidelberg, 69120 Heidelberg, Germany

Pablo Artal

Laboratorio de Optica, Departamento de Física, Universidad de Murcia, Campus de Espinardo (Edificio C), 30071 Murcia, Spain

Received July 29, 1999; revised manuscript received March 20, 2000; accepted April 12, 2000

A description of a Hartmann–Shack sensor to measure the aberrations of the human eye is presented. We performed an analysis of the accuracy and limitations of the sensor using experimental results and computer simulations. We compared the ocular modulation transfer function obtained from simultaneously recorded double-pass and Hartmann–Shack images. The following factors affecting the sensor performance were evaluated: the statistical accuracy, the number of modes used to reconstruct the wave front, the size of the microlenses, and the exposure time. © 2000 Optical Society of America [S0740-3232(00)00108-3]

OCIS codes: 330.5370, 120.3890, 110.3000.

1. INTRODUCTION

For more than two centuries, researchers have been interested in measuring the degradation of the retinal image in the human eye beyond the refractive errors. Although earlier studies dealt mainly with spherical aberration, there was evidence that the eye's aberrations are not axially symmetric. Smirnov¹ pointed out that the wave aberration (WA) function was the most convenient way of describing the performance of ocular optics.

The WA describes the image-forming properties of any optical system² and, in particular, of the human eye. Seidel aberrations, the point-spread function, and the optical transfer function can be computed from the WA. In the case of the human eye, the WA, in addition to its value in completely describing image performance, serves as a tool in ophthalmic design (lenses, contact lenses, and intraocular lenses) and as a possible index for evaluating the eye's optical quality after surgical procedures. The application of adaptive optics techniques in the eye^{3,4} for high-resolution retinal imaging and for improved spatial vision also requires precise estimates of the ocular WA.

There are a variety of techniques to measure the WA in artificial optical systems.⁵ Some are based on direct or indirect estimates of the wave front from data of the pupil plane, e.g., radial shearing interferometry, point-diffraction interferometry, the Foucault knife-edge test, and Hartmann-based sensors. Other techniques use data about the image plane, such as the curvature sensor and computational phase retrieval. These techniques usually involve a single pass through the system from a test source to the detector. In the case of the eye, a single

pass would require placement of either (1) the detector or (2) the light source within the retina. Subjective methods for estimating the WA¹ can be considered in making use of the first technique, since the retina itself is used as a detector. On the other hand, objective methods involve the latter second technique, which produces a light spot on the retina. One objective method is to compute the WA from pairs of double-pass retinal images by phase-retrieval techniques.⁶ Another objective method, appropriate when fast estimates of the aberrations are required, is the Hartmann–Shack (HS) sensor.^{7,8}

In this paper we study a series of factors that affect the performance of the HS sensor in measuring the aberrations of the human eye. We performed simultaneous recording of HS images and the associated double-pass (DP) images and compared the results by means of the modulation transfer function (MTF). We then evaluated different sources that were able to produce a discrepancy between the two image-quality estimates.

2. THEORY

In the Hartmann test, a wave front is sampled in a number of locations by means of an opaque screen with a set of holes placed in the propagation path. As a result, a set of spots is produced on a recording plane. The local slope of the wave front at each sample point can be evaluated from the direction in which most of the light emerges from the corresponding hole, that is, from the spot position. The HS sensor was developed as a means of incrementing the signal-to-noise ratio in the Hartmann test.

The array of holes was replaced by a microlens array. In the focal plane, each microlens produces the Fraunhofer diffraction pattern corresponding to the wave-front section it covers. Owing to the typical microlens size (1 mm or less), these patterns are usually extended spots. For a flat wave front, neglecting microlenses and camera defects, the image will consist of a regular matrix of spots, each one centered in the area associated with the corresponding lens. On the other hand, when the wave front is aberrated, the spot matrix is distorted. As in the Hartmann test, the position of a spot provides information about the local slope of the wave front over each microlens.

Among the possible strategies for positioning an extended spot, we evaluated the center of gravity, or centroid. This technique is widely used since it is fast and easy to perform. The centroid (X_j, Y_j) of the j th spot can be defined as⁹

$$X_j = \frac{\int_{A_j} x I(x, y) dx dy}{\int_{A_j} I(x, y) dx dy}, \quad Y_j = \frac{\int_{A_j} y I(x, y) dx dy}{\int_{A_j} I(x, y) dx dy}, \quad (1)$$

where A_j represents the image area associated with the j th lens and $I(x, y)$ is the image intensity. From this definition, it can be shown that the displacement of the centroid ($\Delta x_j, \Delta y_j$) of the j th spot is proportional to the average of the wave-front derivative across the microlens⁹:

$$\begin{aligned} \Delta x_j &= \frac{f}{A} \int_{A_j} \frac{\partial W(x, y)}{\partial x} dx dy, \\ \Delta y_j &= \frac{f}{A} \int_{A_j} \frac{\partial W(x, y)}{\partial y} dx dy, \end{aligned} \quad (2)$$

with f and A representing the focal length and the area of a single microlens, respectively, and $W(x, y)$ being the WA in radians. These relationships are linear, and therefore if ($\Delta x_j, \Delta y_j$) represent the spot shifts between two recorded images corresponding to different wave-fronts, $W(x, y)$ is replaced by the wave-front difference. This is particularly important when we are interested in isolating the WA associated with an optical element, since the contribution of the rest of the system can be eliminated by using the spot positions on a reference image.

Although different algorithms have been proposed^{10–12} to reconstruct the WA from the averaged derivatives, the most widely used algorithms are modal approaches, consisting of fitting the coefficients for the expansion of the wave front on a specific functional basis. The wave front can be expressed as

$$W(x, y) = \sum_k^{k_{\max}} \zeta_k Z_k(x, y), \quad (3)$$

where $Z_k(x, y)$ denotes the k th mode, ζ_k is its coefficient, and k_{\max} is the expansion truncation mode. We selected the Zernike circle polynomials¹³ as the functional basis for this modal expansion of the WA. Taking partial derivatives in Eq. (3) and integrating across each microlens

area, we show that the mean wave-front slope can also be expressed as a combination of the mode slopes with the same coefficients:

$$\begin{aligned} \int_{A_i} \frac{\partial W(x, y)}{\partial x} dx dy &= \sum_k^{k_{\max}} \zeta_k \left[\int_{A_i} \frac{\partial Z_k(x, y)}{\partial x} dx dy \right], \\ \int_{A_i} \frac{\partial W(x, y)}{\partial y} dx dy &= \sum_k^{k_{\max}} \zeta_k \left[\int_{A_i} \frac{\partial Z_k(x, y)}{\partial y} dx dy \right]. \end{aligned} \quad (4)$$

By combining Eqs. (2) and (4), we obtain two systems of N equations. They relate the measured x - and y -direction displacements of the N spots and the mean x and y partial derivatives of each mode inside each microlens, through the mode coefficients, ζ_k . These two systems can be mixed, since they have the same unknowns, and expressed in matrix notation as

$$\Delta = \mathbf{B}\zeta, \quad (5)$$

with Δ and ζ being column vectors representing the $2N$ spot displacements in the x and y directions and the k_{\max} unknown coefficients, respectively. \mathbf{B} is the $k_{\max} \times 2N$ matrix of partial (x and y) derivatives of the modes, averaged across each microlens. If the number of sampling microlenses is high enough, the system in Eq. (5) is redundant, although in general inconsistent, owing to measurement noise and possible aberration terms of order higher than that of the truncation mode. In that case, least-squares estimates of the coefficients ζ_k are obtained by solving the system. Once the coefficients of the modal expansion are known, the WA is given by Eq. (3).

3. METHODS

A. Experimental Apparatus

An apparatus to simultaneously record HS and DP images was built (a schematic diagram is shown in Fig. 1). It consists of a modified DP system,¹⁴ with the second pass divided into two paths for simultaneous recording of the HS and the DP images. For illumination, He-Ne laser (632.8-nm wavelength) is used. A spatial filter, SF, consisting of a 10× microscope objective and a 25-μm pinhole, provides a point source that is collimated by means of an achromatic doublet (200-mm focal length). An acousto-optic modulator, AOS, allows beam switching for controlling the duration of the exposure. A linear polarizer (producing p -component light), LP, and a revolver of apertures, P1, conjugated with the eye pupil, EP, complete the illumination path. A pellicle beam splitter (BS1) reflects 10% of the beam intensity toward the eye, while the transmitted light is removed from the system by a light trap, LT. A Badal system is used to correct the refractive error of the subject. The arrangement consists of two equal achromatic doublets, L2 and L3 (190-mm focal length), and two mirrors mounted on a moving stage, FC, that increases or decreases the optical path between L2 and L3. The subject is fixed with a bite bar on an XYZ positioning stage. In the second pass, the light coming from the retina passes through FC and BS1 and is divided into two paths by means of a polarizing cube, CBS. The p component is reflected and collected with a 400-mm objective that forms the DP image on the CCD array of a sci-

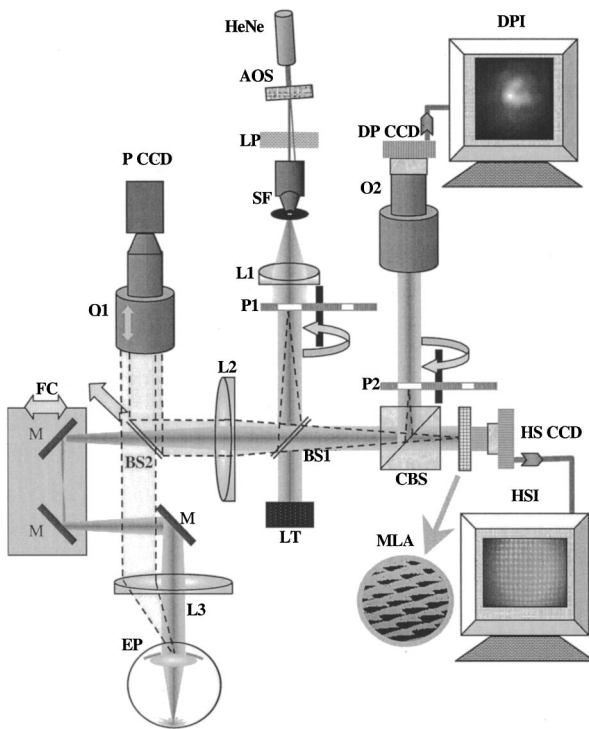


Fig. 1. Experimental setup for simultaneous recording of HS and DP images. See text for a description of the components.

entically cooled CCD camera (Spectra Source MCD1000), DP CCD. A second aperture revolver, P2, conjugated with EP acts as exit pupil. The s component transmitted by CBS is sampled by the microlens array, MLA (square geometry, 53-mm focal length; single micro-lens aperture of 0.4 mm). A second cooled CCD camera (Photometrics-Sensys KAF0400), HS CCD, placed at the focus location of the MLA records the HS images.

To ensure pupil conjugation, the eye pupil, EP, is placed on the focus of L3 while the entrance pupil of the system, P1, and the exit pupil for the DP path, P2, are placed on the focus of L2. The correct pupil locations are controlled with a video camera (P CCD), permitting simultaneous monitoring of the pupils P1, P2, and EP (BS2 can be either a mirror or a beam splitter, which is removed during the measurements). In the experiments, entrance pupil sizes 4 mm or 1.5 mm in diameter were selected with P1, and the DP exit pupil, P2, always had a 4-mm diameter. For measuring the WA in the eye pupil plane, MLA has to be conjugated with EP, and therefore the array is also placed on the focus of lens L2. No artificial pupil is placed in the HS path, and therefore EP acts as exit pupil. This arrangement increases the number of visible spots in the HS image. When the image is being processed, the WA is estimated from the spots included in a circle that corresponds to the desired synthetic pupil. To produce the WA over the DP exit pupil, the synthetic pupil has to be equal to or larger than this pupil. To synchronize the DP and HS measurements and to minimize subject exposure, the AOS and the shutters of both CCD cameras are driven by a common, single transistor-transistor-logic signal. The cumulative error in the whole synchronizing process is less than 2.5 ms. When the AOS is off, its transmittance is 0.01%. This provides

enough light for the subject to use the pinhole of the SF as a fixation target while waiting for the exposure. A series of measurements were obtained with exposure times of 4, 2, 1, 0.5, 0.25, 0.1, and 0.05 s. In every case the total light energy entering the eye was below 0.4 μ J, approximately three orders lower than the American National Standards Institute maximum permissible exposures.¹⁵

Two subjects were studied: PA (male, 36 years old, -2-D myopia) and IH (female, 25 years old, +0.75-D hyperopia). The accommodation was paralyzed and the pupil dilated with tropicamide 1%.

To calibrate the HS sensor, the WA's in an artificial eye and in one trained subject (PA) was measured with several known amounts of additional defocus introduced with the FC. Differences between the theoretical and the measured defocus were less than 3% in all cases.¹⁶ To compare the MTF's, we studied each subject in two different focus positions (best focus and 0.4-D defocus).

B. Modulation Transfer Function Calculations

MTF's were calculated both from the WA estimated with the HS sensor (HS MTF), and from the DP images (DP MTF). The DP image is the autocorrelation of the retinal image.¹⁷ Therefore the DP MTF is the square root of the Fourier transform of the aerial image. On the other hand, to calculate the HS MTF, the WA estimate provided by the HS sensor, $W(x, y)$, is first used to construct the generalized pupil function, $P(x, y)$:

$$P(x, y) = p(x, y)\exp[iW(x, y)], \quad (6)$$

where $p(x, y)$ denotes a pupil aperture of radius R , defined as

$$p(x, y) = \begin{cases} \frac{1}{\pi R^2} & \text{if } x^2 + y^2 \leq R^2 \\ 0 & \text{otherwise} \end{cases}. \quad (7)$$

The MTF (HS MTF) is the modulus of the OTF, obtained as the complex autocorrelation of $P(x, y)$:

$$\text{OTF}(x, y) = \int P(x', y')P^*(x' - x, y' - y)dx'dy'. \quad (8)$$

C. Calculation of the Wave Aberration from the Hartmann-Shack Images

1. Centroiding: Pyramidal and Subpixel Algorithm

The image produced by the array of microlenses is recorded and converted into a digital image to be processed. Estimates of the spots' centroid location, \tilde{X}_j and \tilde{Y}_j , are obtained by replacing the intensity integrals across the j th lens in Eqs. (1) with sums across the pixels (n_x, n_y) inside the area associated with this lens:

$$\tilde{X}_j = \frac{\sum_{(n_x, n_y) \in A_j} n_x I(n_x, n_y)}{\sum_{(n_x, n_y) \in A_j} I(n_x, n_y)},$$

$$\tilde{Y}_j = \frac{\sum_{(n_x, n_y) \in A_j} n_y I(n_x, n_y)}{\sum_{(n_x, n_y) \in A_j} I(n_x, n_y)}. \quad (9)$$

There is an implicit assumption in the definition of Eq. (1) that the intensity of one spot is considered to be confined in the area associated with the corresponding microlens. However, the diffraction pattern corresponding to the microlens aperture extends to infinity, and therefore the confining assumption is well founded only if the intensity is reduced to a negligible value at the edges of the associated area. This may not be the case if the microlens's numerical aperture is small, producing extended diffraction patterns, or if the aberration to be measured presents a high mean slope across any of the microlenses. With large spot displacement, causing the j th spot to extend outside the area A_j and enter into the area corresponding to a neighboring lens, A_k can produce errors in the centroid location. Setting an intensity threshold for estimating the centroid can reduce this problem. For symmetrically shaped spots, this threshold does not change the centroid position.

On the other hand, spot overlapping, or crossover, can be reduced by masking the neighbor microlenses. This expands the associated area A_j , but as a counterpart, either it reduces the number of data or a scanning in masking positions for considering all the microlenses inside the pupil will be required. An alternative solution is the use of a window smaller than A_j for estimating the centroid of the j th spot. It has the advantage of reducing the possible contributions of the tails of neighbor spots, and hence it eliminates one source of bias. However, the smaller the window, the more difficult to ensure that the spot is confined in it.

We used the following strategy to obtain centroid positions: The estimates of \tilde{X}_j and \tilde{Y}_j were iteratively evaluated in windows of decreasing size, each centered on the previous estimate. The first window was the whole area associated with the j th pixel, and the last one was usually the theoretical size of the first lobe of the diffraction pattern corresponding to a square lens. Between these two values, successive windows were used, each one typically one pixel smaller than the previous one. The last window should be centered very close to the actual spot center, and therefore the last centroid estimate should contain no bias that is due to tail asymmetries. The window centering can be refined with a number of iterations using the last window size. The spot center resembles an equilibrium point, since any displacement of the window will produce centroid estimates displaced against this movement, and a few iterations will restore the centering.

When this iterative search procedure is used, some bias can arise if window size and position are rounded to integer pixel numbers. For example, two windows differing

by one pixel in size cannot have the same center, and therefore asymmetries in the spot tails can easily appear. In some cases these asymmetries cause centroid estimates to be slightly incorrect. To overcome this problem, the proposed algorithm does not round sizes and positions but works with floating point numbers of pixels. If Eqs. (9) are understood as the center of gravity of a set of point bodies each centered in the center of the corresponding pixel, the contribution of a fractional part of one pixel can be evaluated by correcting the intensity and the position of the corresponding point body. We considered the pixel intensity as being uniformly distributed inside the pixel area. Hence the fractional intensity was assumed to be the corresponding fraction of the pixel intensity, placed on the center of the fractional part. A point (x, y) is considered to be inside pixel (n_x, n_y) if $n_x - 0.5 \leq x \leq n_x + 0.5$ and $n_y - 0.5 \leq y \leq n_y + 0.5$. Because of the relatively high resolution of our spot images, this assumption about the intensity distribution inside one spot has proved to be valid. More elaborated models for this distribution (e.g., ramp distribution based on neighbor intensities) are not of interest since they increase computational requirements without producing noticeable improvements in spot positioning. However, this kind of processing may be required for lower-resolution images, where the spot size is close to the pixel size and large intensity variations can occur within the area of a single pixel.

2. Wave-Front Reconstruction

Once the spots have been positioned, their x - and y -direction displacements are evaluated and introduced into the system of Eq. (5). First, matrix \mathbf{B} of the mean mode derivatives has to be evaluated. We chose Noll's¹³ definition for ordering and normalizing the Zernike circle polynomials. The radial degree, n , and the azimuth frequency, m , for the k th polynomial in this ordering can be obtained as

$$n = \text{Int}\left(\frac{-1 + \sqrt{8k - 7}}{2}\right),$$

$$m = \begin{cases} 2 \text{Int}\left[\frac{k}{2} - \frac{n(n+1)}{4}\right] & \text{if } n \text{ is even} \\ 1 + 2 \text{Int}\left[\frac{k-1}{2} - \frac{n(n+1)}{4}\right] & \text{if } n \text{ is odd} \end{cases}, \quad (10)$$

where the function $\text{Int}()$ gives the nearest integer number that is smaller than the parenthesis. From these two parameters, n and m , Noll defined the k th Zernike polynomial using radial coordinates, (r, θ) , as

$$Z_k(r, \theta) = \begin{cases} \sqrt{n+1} R_n^0(r) & \text{if } m = 0 \\ \sqrt{n+1} R_n^m(r) \sqrt{2} \cos(m\theta) & \text{if } m \neq 0 \text{ and } k \text{ is even,} \\ \sqrt{n+1} R_n^m(r) \sqrt{2} \sin(m\theta) & \text{if } m \neq 0 \text{ and } k \text{ is odd} \end{cases} \quad (11)$$

where the radial polynomials $R_n^m(r)$ are

$$R_n^m(r)$$

$$= \sum_{s=0}^{(n-m)/2} \frac{(-1)^s (n-s)!}{s![(n+m)/2-s]![(n-m)/2-s]!} r^{n-2s}. \quad (12)$$

However, for our purposes it is more appropriate to use rectangular coordinates, (x, y) , for $Z_k(x, y)$:

$$Z_k(x, y) = \begin{cases} \sqrt{n+1} \sum_{b=0}^{n/2} \sum_{c=0}^{n/2-b} (-1)^b \frac{(n-b)!}{b!(n/2-b)!(n/2-b-c)!c!} x^{n-2b-2c} y^{2c} & \text{if } m = 0 \\ \sqrt{2(n+1)} \sum_{a=0}^{\text{Int}(m/2)} \sum_{b=0}^{(n-m)/2} \sum_{c=0}^{(n-m)/2-b} (-1)^{a+b} \binom{m}{2a} \\ \times \frac{(n-b)!}{b![(n+m)/2-b]![(n-m)/2-b-c]!c!} x^{n-2a-2b-2c} y^{2a+2c} & \text{if } m \neq 0 \text{ and } k \text{ even.} \\ \sqrt{2(n+1)} \sum_{a=0}^{\text{Int}((m-1)/2)} \sum_{b=0}^{(n-m)/2} \sum_{c=0}^{(n-m)/2-b} (-1)^{a+b} \binom{m}{2a+1} \\ \times \frac{(n-b)!}{b![(n+m)/2-b]![(n-m)/2-b-c]!c!} x^{n-2a-2b-2c-1} y^{2a+2c+1} & \text{if } m \neq 0 \text{ and } k \text{ odd} \end{cases} \quad (13)$$

When these expansions of the Zernike polynomials for the square geometry of the microlens array are used, the integrals in the right-hand side of Eqs. (4), i.e., the elements of matrix \mathbf{B} in expression (5), are expressed as a simple analytic function of the microlens edge positions. They are referred to the pupil center since this is the origin of coordinates for the Zernike polynomial basis. Depending on the microlens size and the shape of the polynomial considered, these integrals are sensitive to edge position changes that are due to lateral displacements of the microlens array with respect to the pupil. Therefore, in order to evaluate matrix \mathbf{B} correctly, we need to determine the relative positioning of the microlens array and of the pupil. Each element of \mathbf{B} represents the mean slope of a single Zernike polynomial (by columns) across one microlens in the x or the y direction (by rows). We ordered the microlenses from top to bottom and from left to right and placed all the x -direction derivatives in rows 1 to N and the y direction derivatives in rows $N+1$ to $2N$. However, it is important to note that the solution of the system is independent of changes in this ordering and (except for noise artifacts) is also independent of the elimination of some rows, provided that the vector Δ has been constructed in a manner consistent with the number and ordering of the elements considered. This permits us to obtain an accurate estimation of the wave front even when some of the spots are missing in the HS image. In other words, the algorithm is robust with incomplete data. Moreover, a particular subset of the mode coefficients, not necessarily sequential, could be selected by using only the corresponding columns in matrix \mathbf{B} .

4. RESULTS

A. Comparison of Double-Pass and Hartmann-Shack Estimates of the Ocular Modulation Transfer Function

Figures 2 and 3 show the one-dimensional MTF's (radially averaged) for subjects PA and IH, respectively, at (a) the best focus and (b) for a specific residual focus error. In every case the HS MTF is higher than the DP MTF, although in the defocused case the two functions tend to become similar. While the DP method may produce slightly lower estimates of the retinal image

quality,¹⁸ the HS sensor tends to render WA estimates smoother than the actual one when long exposure times

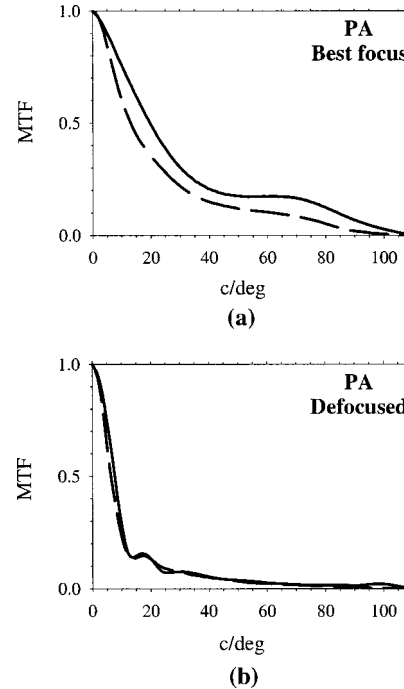


Fig. 2. Comparison between radially averaged MTF estimates obtained from DP images (DP MTF, dashed curves) and from WA estimates provided by HS (HSMTF, solid curves) for subject PA at two focuses.

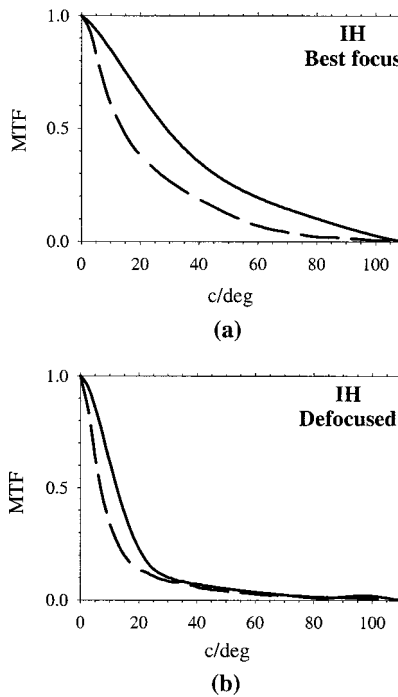


Fig. 3. Comparison between radially averaged MTF estimates obtained from DP images (DP MTF, dashed curves) and from WA estimates provided by HS (HS MTF, solid curves) for subject IH at two focuses.

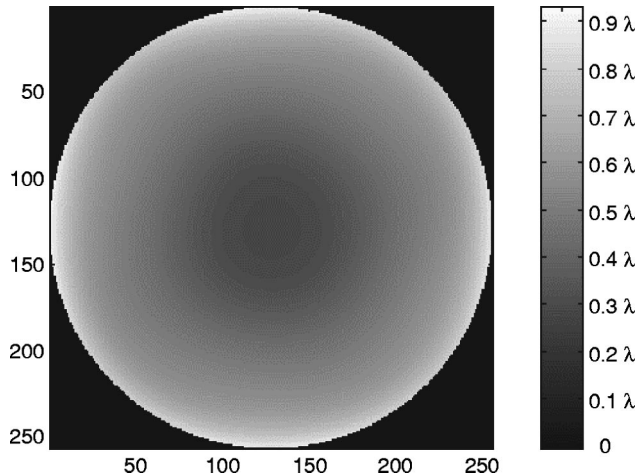


Fig. 4. Gray-scale image representing the statistical fluctuations of the WA estimation algorithm when a series of random x and y displacements (equiprobable distribution between $[-1, 1]$ pixel) are introduced. The gray level at each point represents the standard deviation of the WA value in a set of 10,000 simulations.

are used. This point will be further discussed in Subsections 4.A and 4.B, and it results in an overestimation of the MTF.

B. Statistical Accuracy of the Hartmann–Shack Sensor
To estimate the statistical accuracy of the HS sensor, we introduced a series of random data into the modal fitting algorithm. This is analogous to an experiment in which a flat wave front is detected with random errors in the centroid detection. Owing to the linearity of the wave-front estimate, this result can be extended to any other

WA shape. Figure 4 represents, as a gray-level image, the typical deviation of the wave-front estimation when equiprobable random fluctuations in the range of $[-1, 1]$ pixels are introduced. To perform this simulation, we considered the specifications of our HS sensor (see Subsection 3.A) operating with a 4-mm pupil diameter. The fluctuations in the WA increase radially, but the WA statistical error barely exceeds $\lambda/10$ at the pupil edge. Table 1 shows the mean values and standard deviations for the first 15 Zernike modes. Figure 5 shows the radial average of the standard deviation for different ranges of centroiding errors. Although it is difficult to quantify the actual positioning error in the HS sensor, an error of $[-1, 1]$ pixel is by far the highest limit for the fluctuation range when a subpixel centroiding algorithm is used.

C. Spatial Resolution of the Hartmann–Shack Sensor

A limited spatial resolution in the HS sensor would produce a smoother WA. This would lead to an overestimation of the image quality of the system and could explain some of the discrepancies between the HS MTF and the DP MTF.

Two different, although related, factors limit the spatial resolution of the WA estimates obtained from the HS data:

1. The microlens size. Each lens of the array acts as a spatial integrator, and therefore details smaller than its size cannot be captured.
2. The number of modes used to express the WA. This number is always limited, sometimes owing to computational considerations and ultimately owing to the number of data available for fitting, and this truncation of the WA expansion results in a loss of higher-order details.

To evaluate the effect of the microlens size on the estimation of the WA, we performed an additional computer simulation, in which the HS spot-decentering data corresponding to a known WA were evaluated for the same pupil diameter with arrays of square microlenses of different sizes. If the microlens size had an impact on the

Table 1. Mean Value and Standard Deviation in the First 15 Zernike Modes for the Simulation Testing the Statistical Accuracy of the HS Sensor for 1000 Events with a Random Probability of $[-1, 1]$ Pixels in the Centroid Positioning

Zernike Index	Mean Value (in λ)	Standard Deviation (in λ)
4	0.0001157	0.016
5	-0.000129	0.0225
6	-0.0005658	0.0219
7	0.0000273	0.0124
8	0.000592	0.0125
9	0.0001128	0.0179
10	-0.000705	0.0176
11	-0.0003231	0.0116
12	0.0003653	0.0119
13	0.0001352	0.011
14	0.0001658	0.016
15	-0.0004611	0.0155

sensor's spatial resolution, the smaller the microlenses, the better the resolution should be. As a side effect, the number of data increases since the pupil is sampled with a higher number of lenses. The WA used in the simulation was obtained from a set of randomly generated Zernike coefficients of decreasing magnitude with increasing order, which is consistent with a typical eye's WA for a medium-to-severe case. Figure 6 shows the first Zernike coefficients of the original WA and those reconstructed with different microlens sizes. The fitting was performed up to sixth order, and the results are quite stable for sensor configurations with microlens size 1/8 of the pupil diameter or smaller. Discrepancies appear only when the number of lenses is too low for an accurate

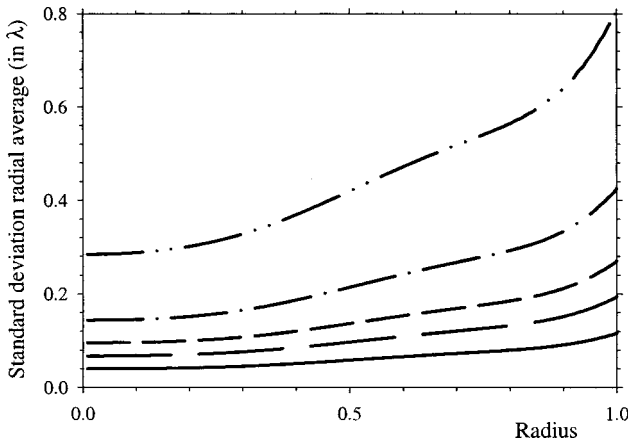


Fig. 5. Radial average of the standard deviation of the WA estimates provided by the algorithm when a series of equiprobable random x and y displacements are introduced for different fluctuation amplitudes. Solid curve, $[-1, 1]$ pixel; long-dashed curve, $[-2, 2]$ pixels; short-dashed curve, $[-3, 3]$ pixels; dashed-dotted curve, $[-5, 5]$ pixels; dashed-double-dot curve, $[-10, 10]$ pixels.

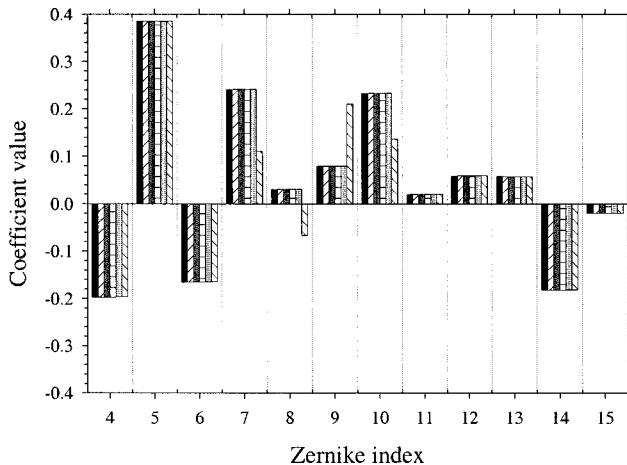


Fig. 6. Simulation of the performance of HS sensors with different spatial sampling. The black bar represents the first 15 randomly generated coefficients for the Zernike expansion of a WA (100 coefficients were simulated with Gaussian distribution to obtain realistic values). The other bars represent the result of a sixth-order fitting when the WA is sampled with microlens arrays of decreasing resolution: forward-slash bar, 24×24 microlenses inside the pupil; dark-gray bar, 16×16 ; horizontally dashed bar, 12×12 ; light-gray bar, 8×8 ; back-slash bar, 6×6 . Only the first 15 of 35 coefficients are plotted.

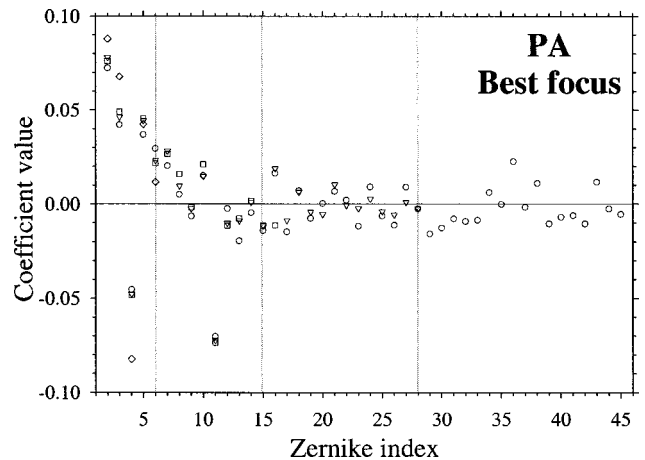


Fig. 7. Results of processing the spot image obtained for subject PA at best focus with different numbers of Zernike polynomials. Diamonds, fitting up to second order; squares, fitting up to fourth order; triangles, fitting up to sixth order; circles, fitting up to eighth order. Vertical gray lines show the last coefficient in each fitting.

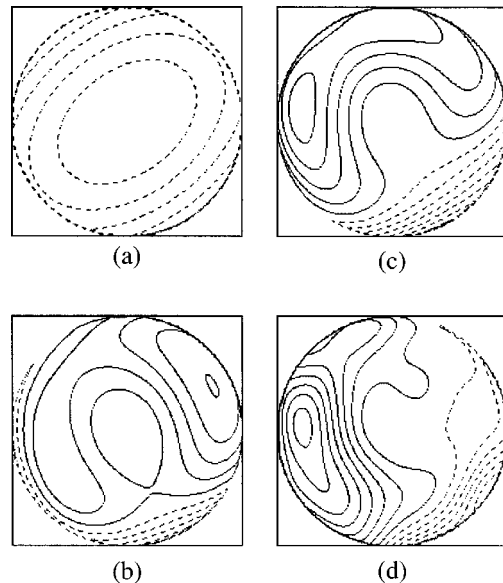


Fig. 8. Contour plots of the successive estimates of the WA of subject PA at best focus, each one obtained from the corresponding set of coefficients shown in Fig. (7). (a) Fitting up to second order, (b) fitting up to fourth order, (c) fitting up to sixth order, (d) fitting up to seventh order.

fitting with the required number of modes. This stability suggests that the spatial resolution of the HS sensor is not affected primarily by the lens size, provided that the total number of active lenses is large enough to fit the desired number of coefficients.

The other factor potentially affecting the WA reconstruction is the number of fitted coefficients.¹⁹ We processed the HS images for subject PA, changing the number of fitted coefficients. Figure 7 shows the values of the coefficient obtained when the fitting was performed up to second order (5 modes), fourth order (14 modes), sixth order (27 modes) and eighth order (44 modes). Except for the first case, the coefficients obtained are rather tolerant to the number of terms considered. Figure 8 shows a se-

ries of WA maps for subject PA in best focus fitted with different numbers of modes. Figures 9 and 10 compare the MTF's corresponding to the different-order WA estimates for subject PA and the MTF estimated from the DP image. For both the best focus and the defocused cases, the HS MTF becomes closer to the DP MTF when the number of modes is increased. This means that the use of a limited number of modes actually produces a loss of spatial resolution and consequently an overestimation of the image quality of the system. However, very small variations occurred in the HS MTF curves above the fourth order. This suggests that, at least for this subject, fourth order is good enough to deal with the main part of the eye aberrations with a 4-mm pupil diameter, in good agreement with Liang and Williams.⁸ For the best-focus case, a gap remains between the HS MTF and the DP MTF, even when the highest order was fitted, whereas for the defocused case the MTF's are very similar except for the lower-order fitting. This behavior can be explained by the different impacts that the fluctuations of the eye WA have in each estimate of the MTF. This point is analyzed in Subsection 4.D.

D. Temporal Fluctuations and Exposure Time

DP system theory is based on the assumption of incoherence for the retinal reflection. When this condition is fulfilled, the second pass can be considered as being independent from the first pass. In DP imaging with equal-sized entrance and exit pupils, this independence allows us to obtain the single-pass MTF as the square root of the DP MTF. With the HS sensor, it allows us to isolate the second-pass WA, since the retinal image for the first pass only blurs the HS spots but does not locally change their

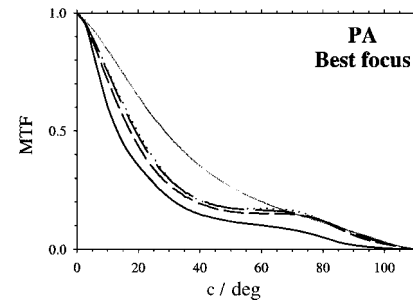


Fig. 9. Comparison between MTF estimates for subject PA at best focus, obtained from DP images (DP MTF, solid black curve) and from WA estimates provided by HS with different numbers of Zernike coefficients (HS MTF from WA up to second order, solid gray curve; up to fourth order, dotted curve; up to sixth order, long-dashed curve; up to eighth order, short-dashed curve).

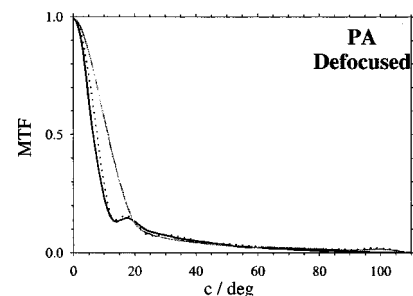


Fig. 10. Comparison between MTF estimates for subject PA in a defocused case, obtained from DP images (DP MTF, solid black curve) and from WA estimates provided by HS with different numbers of Zernike coefficients (HS MTF from WA up to second order, gray curve; up to fourth order, dotted curve).

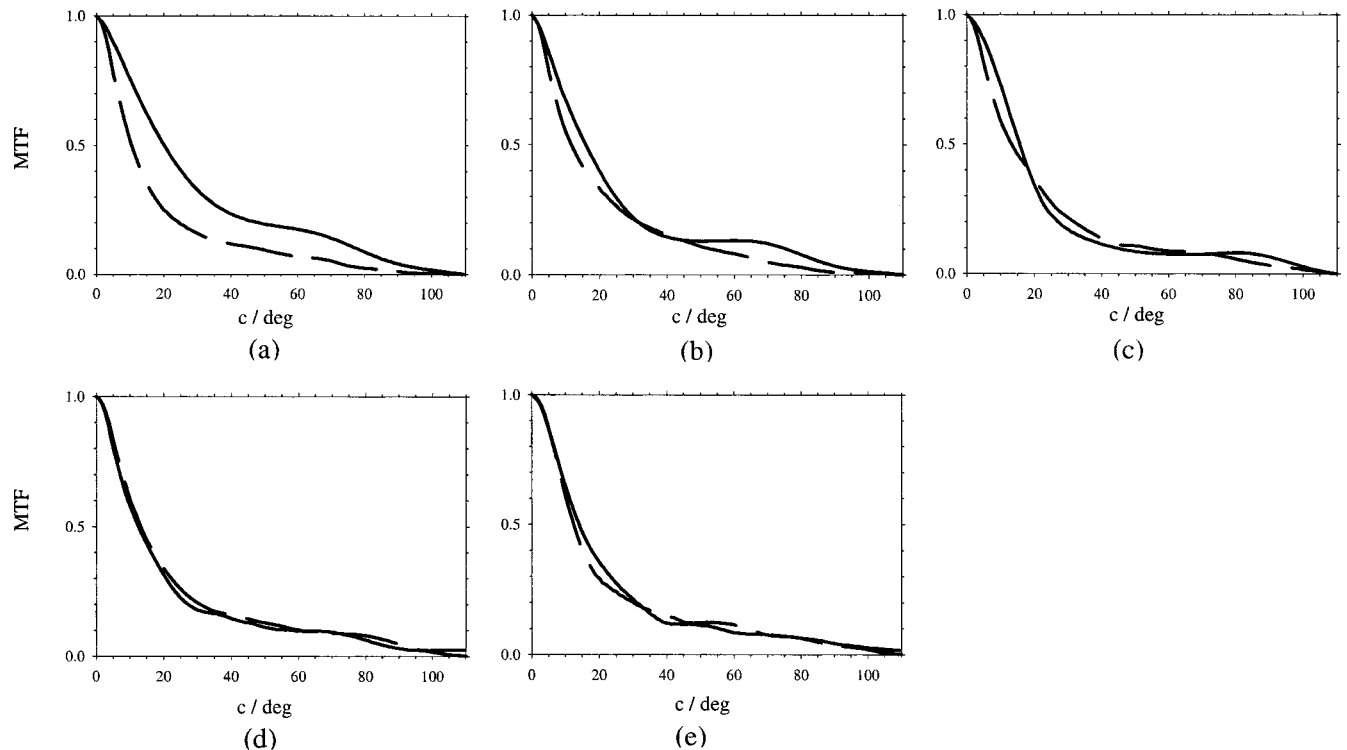


Fig. 11. Comparison between radial average of the MTF estimates obtained from DP images (DP MTF, dashed curve) and from WA estimates provided by HS (HS MTF, solid curve) for subject PA in best focus and for different exposure times: (a) 2 s, (b) 1 s, (c) 0.5 s, (d) 0.25 s, (e) 0.1 s.

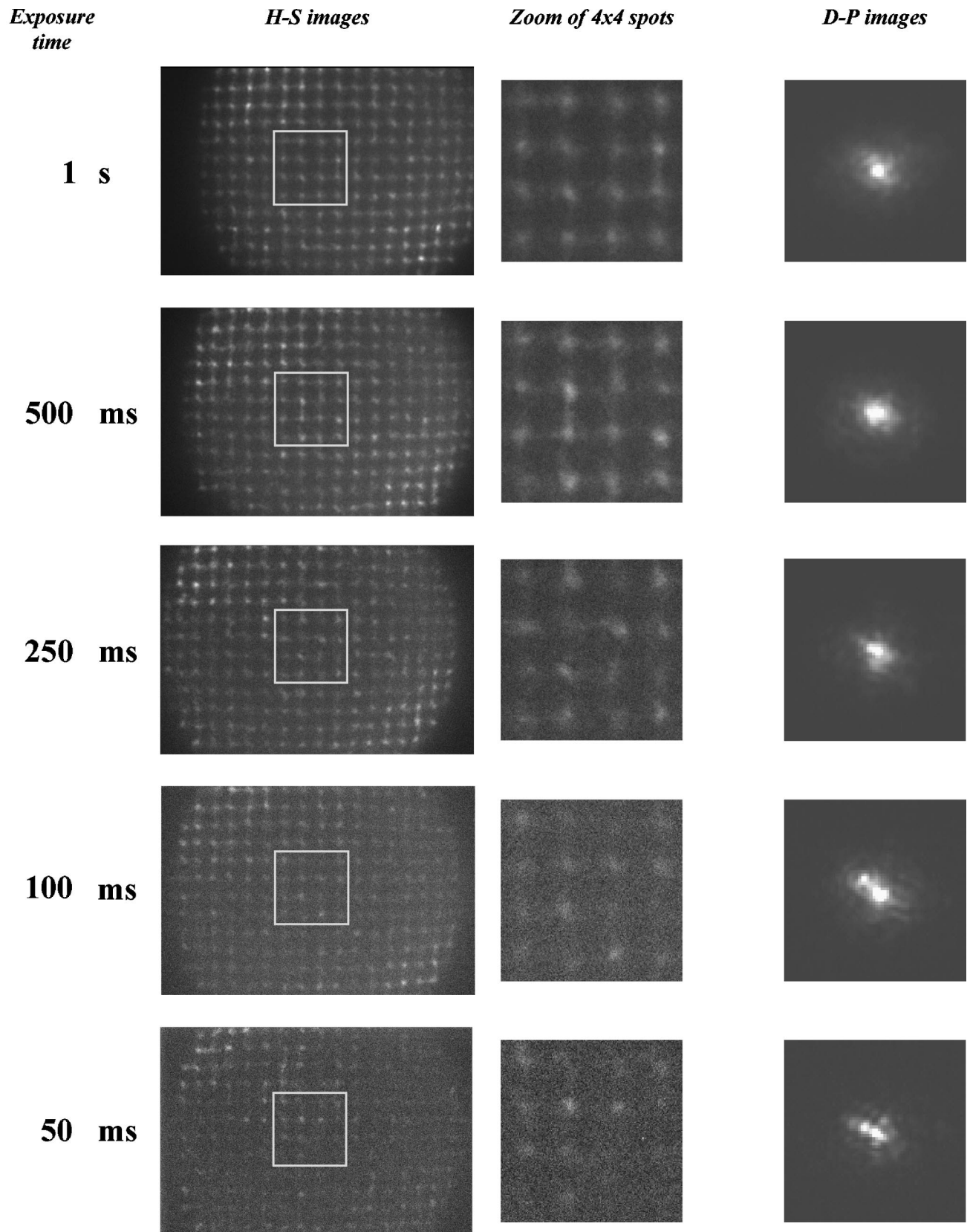


Fig. 12. Comparison between HS and DP images for different exposure times. For each exposure time studied we display the total 768×512 pixel HS image, a zoomed 178×178 pixel area (corresponding to 4×4 spots, i.e., 1.6×1.6 mm), and a 100×100 section of the DP image (corresponding to a field of 23 arc min).

positions. If the incoherence is not secured, the parts of the light pathway through the system (first-pass, reflection, and second-pass) cannot be completely isolated. The single-pass MTF cannot be easily obtained from the total MTF, and the HS sensor provides a total DP WA instead of the single-pass WA. With coherent illumination, eye movements can be exploited to produce incoherent reflection if long exposure times are used, typically longer than 1 s. As a counterpart, during long recording time, the eye WA fluctuates²⁰ and both DP and HS images are temporal averages. This averaging process has opposite consequences on DP and HS measurements. While fluctuations of the eye's aberrations tend to blur the DP image, leading to a reduction in the MTF, the mean WA can be smoother than the individual instantaneous WA's, indicating a higher image quality. This different behavior can explain both the differences in the MTF's of Figs. 2(a) and 3(a) and those observed in the defocused case, where a large amount of static extra aberration is present.

As a test of this temporal averaging effect, DP and HS images for subject PA were recorded for different exposure times: 4, 2, 1, 0.5, 0.25, 0.1, and 0.05 s. Figure 11 shows the DP MTF and the HS MTF for exposure times from 0.1 to 2 s [Fig. 2(a) shows the MTF's for 4 s recording time]. The two MTF's are very similar for the shorter exposure times, but a difference appears for the longer times. These results agree with the previous prediction of a different behavior of the temporal averaging.

The kinds of problems that appear when short exposure times are used in combination with coherent illumination are evident in the series of HS and DP images shown in Fig. 12. The high-contrast speckle patterns in the short-exposure images show that coherence is not broken. Also, it is important to note that for the shortest times neither the MTF nor the WA results can be considered good estimates of a single pass through the eye optics, since incoherent retinal reflection was not secured. The MTF estimates correspond, therefore, to a more complex system involving both passes and the retinal reflection. However, this problem can be solved by externally breaking the coherence. Hofer *et al.*²¹ proposed a method to remove speckle by scanning the retinal image during the recording time. Another alternative for reducing speckle is the use of short coherence sources.²⁰ With those methods, the instantaneous image quality corresponding to a single pass through the eye optics can be estimated.

5. SUMMARY

We have analyzed the performance of the HS sensor in estimating the image quality of the eye. For this purpose, we simultaneously recorded HS and DP images under the same optical conditions and compared the MTF's. The DP method produces lower estimates of retinal image quality than the HS sensor does. We analyzed several possible factors in order to understand these discrepancies and to evaluate the performance of the HS sensor in the eye.

First, a computer simulation was performed to estimate the statistical accuracy of the HS sensor. For the parameters of our sensor, small errors arise from the sta-

tistical fluctuations that can be introduced in the centroiding as a result of noise in the spot image. Therefore the discrepancies in the image-quality estimates cannot be explained in terms of statistical errors in the measurements. Second, the spatial resolution of the HS sensor was analyzed. Spatial resolution is limited by the micro-lens size and/or by the number of modes used to fit the WA. An additional computer simulation showed that eventually the limiting factor is the latter, since once the number of modes has been fixed, the number of lenses does not affect the fitting results, provided that the number of data was enough to overdetermine the system in Eq. (5). However, slight differences in the MTF's were found when the number of modes was increased, suggesting a relatively minor relevance for the higher-order aberrations for 4-mm pupils. Third, the effects of time averaging were studied, by recording simultaneously DP and HS images within a range of exposure times. The differences between the HS and DP estimates of the ocular MTF become smaller, and even negligible, for short exposure times. This suggests that the temporal fluctuations of the WA over the long exposure times that are required to break the coherence of retinal reflection may be responsible for some of the discrepancies found between the DP and HS estimates of the MTF.

ACKNOWLEDGMENTS

This research was supported by Dirección General de Enseñanza Superior (DGES) grant PB97-1056, Acción integrada-HA96-22, and German-Bi257/17-2. The authors thank A. Tuerpitz, F. Mueller, and J. F. Bille of the University of Heidelberg, Germany, for their contributions to the earlier stages of this work. E. Berrio and J. L. Aragón helped in some parts of the work. The experiments reported in this paper were performed during the years 1997–1998 at the University of Murcia. However, an important part of the ideas related to the HS image analysis presented here, i.e., pyramidal centroid detection, selectable spots, and variable number of Zernike modes in the reconstruction, were developed as a collaborative effort with D. Williams and his laboratory when one of the authors (P. Artal) was on sabbatical at the University of Rochester. The final writing of the manuscript was also completed in Rochester. P. Artal is indebted to D. Williams and members of his group for helpful comments and discussion.

Address correspondence to Pablo Artal at the address on the title page or by e-mail: pablo@fcu.um.es.

REFERENCES

1. M. S. Smirnov, "Measurement of the wave aberration of the human eye," *Biophysics* **6**, 776–794 (1961).
2. M. Born and E. Wolf, *Principles of Optics* (Pergamon, New York, 1985).
3. J. Liang, D. R. Williams, and D. T. Miller, "Supernormal vision and high-resolution retinal imaging through adaptive optics," *J. Opt. Soc. Am. A* **14**, 2884–2892 (1997).
4. F. Vargas-Martín, P. Prieto, and P. Artal, "Correction of the aberrations in the human eye with liquid-crystal spatial light modulators: limits to the performance," *J. Opt. Soc. Am. A* **15**, 2552–2562 (1998).

5. D. Malacara, *Optical Shop Testing*, 2nd ed. (Wiley, New York, 1992).
6. I. Iglesias, E. Berrio, and P. Artal, "Estimates of the ocular wave aberration from pairs of double-pass retinal images," *J. Opt. Soc. Am. A* **15**, 2466–2476 (1998).
7. J. Liang, B. Grimm, S. Goelz, and J. F. Bille, "Objective measurement of WA's of the human eye with the use of a Hartmann-Shack wave-front sensor," *J. Opt. Soc. Am. A* **11**, 1949–1957 (1994).
8. J. Liang and D. R. Williams, "Aberrations and retinal image quality of the normal human eye," *J. Opt. Soc. Am. A* **14**, 2873–2883 (1997).
9. G. Rousset, "Wavefront sensing," in *Adaptive Optics for Astronomy*, D. M. Alloin and J.-M. Mariotti, eds. (Kluwer Academic, Dordrecht, The Netherlands, 1994).
10. R. Cubalchini, "Modal wave-front estimation from phase derivative measurements," *J. Opt. Soc. Am.* **69**, 972–977 (1979).
11. W. H. Southwell, "Wave-front estimation from wave-front slope measurements," *J. Opt. Soc. Am.* **70**, 998–1006 (1980).
12. F. Roddier and C. Roddier, "Wavefront reconstruction using iterative Fourier transforms," *Appl. Opt.* **30**, 1325–1327 (1991).
13. R. J. Noll, "Zernike polynomials and atmospheric turbulence," *J. Opt. Soc. Am.* **66**, 207–211 (1976).
14. J. Santamaría, P. Artal, and J. Bescós, "Determination of the point-spread function of the human eye using a hybrid optical-digital method," *J. Opt. Soc. Am. A* **4**, 1109–1114 (1987).
15. American National Standard for the Safe Use of Lasers, Rep. ANSI Z136.1 (Laser Institute of America, Orlando, Fla., 1993).
16. F. Vargas-Martín, "Optica adaptativa en oftalmoscopia: corrección de los aberraciones oculares con un modulador espacial cristal líquido," Ph.D. Thesis (University of Murcia, Murcia, Spain, 1999).
17. P. Artal, S. Marcos, R. Navarro, and D. R. Williams, "Odd aberrations and double-pass measurements of retinal image quality," *J. Opt. Soc. Am. A* **12**, 195–201 (1995).
18. D. R. Williams, D. H. Brainard, M. J. McMahon, and R. Navarro, "Double-pass and interferometric measures of the optical quality of the eye," *J. Opt. Soc. Am. A* **11**, 3123–3134 (1994).
19. J. Herrmann, "Cross coupling and aliasing in modal wave-front estimation," *J. Opt. Soc. Am.* **71**, 989–992 (1981).
20. H. J. Hofer, P. Artal, J. L. Aragón, and D. R. Williams, "Temporal characteristics of the eye's aberrations," *Invest. Ophthalmol. Visual Sci. Suppl.* **40**, S365 (1999).
21. H. J. Hofer, J. Porter, and D. R. Williams, "Dynamic measurement of the wave aberration of the human eye," *Invest. Ophthalmol. Visual Sci. Suppl.* **39**, S209 (1998).